

The art and science of translucent color organic solar cells

Received: 22 August 2024

Accepted: 6 January 2025

Published online: 11 January 2025



Baozhong Deng^{1,6}, Yi Li^{1,6}, Zhouyi Lu¹, Kaiwen Zheng¹, Tao Xu¹✉, Shenghao Wang², Xiaoshu Luo³, Bruno Grandidier⁴, Jianhua Zhang¹✉ & Furong Zhu⁵✉

The artistic and scientific perspectives of the translucent color organic solar cells (OSCs), made with the emerging narrowband nonfullerene acceptors are explored. The translucent color OSCs, comprising a Fabry–Pérot microcavity optical coupling layer, have a power conversion efficiency of >15% and a maximum transparency of >20% for the three primary colors. The performance–color relationship of the translucent color OSCs is analyzed using a combination of high-throughput optical computing and experimental optimization, allowing light with desired color to pass through, while absorbing enough light to generate electricity. Replication of Piet Mondrian’s artwork “Composition C (1920)” is demonstrated using a 10 × 10 cm²-sized translucent OSC module with a wide palette of colors and hues. The outcome of the work offers an opportunity for translucent color OSCs to function as both esthetic art and power generating windowpanes for use in our homes, offices, and even greenhouses.

Energy consumption in buildings accounts for more than a third of world electricity use. It motivates innovation in the development of advanced sustainable energy technologies, including emerging solution-processable solar cells and building-integrated photovoltaics (BIPV)^{1–5}. To date, the application of BIPV is dominated by silicon-based opaque solar cell modules, which cannot make full use of the building facade^{6,7} and do not have a very high degree of esthetic appeal. In comparison, organic solar cells (OSCs) that use solution-based processing technologies are simpler and less expensive to make. The flexibility, color and semi-transparency features also add a decorative and esthetic dimension to the OSCs that can be blended seamlessly into the overall BIPV design. In this respect, semitransparent organic solar cells (ST-OSCs) have emerged as a promising complement to power-generating windows, outperforming conventional silicon solar cell panels because of the selective near-infrared (NIR) absorption of organic semiconductors to benefit simultaneously the power conversion and visible transparency^{8–12}. The development of ST-OSCs is

progressing rapidly due to the innovation in absorbing materials, such as nonfullerene acceptors (NFAs) that exhibit improved absorption in the NIR wavelength range^{13–17}, resulting in enhanced power conversion efficiency (PCE) of 13–15% and average visible transmittance (AVT) of 30–40%^{18–22}. In parallel, significant improvements on the performance of ST-OSCs has been achieved using high-throughput computing guided low/high index optical coupling layer for maximizing the absorption of NIR electromagnetic waves^{23–26}. A ST-OSC is essentially a weak thin film microcavity system. By incorporating a pair of front transparent electrode and a rear metal/dielectric spacer layer/metal optical coupling layer^{27–31}, its color appearance can be adjusted by modulating the resonance mode of the Fabry–Pérot microcavity.

Therefore, considerable research efforts have been devoted to exploring BIPV from photovoltaic and artistic perspectives. For instance, the creation of translucent color OSCs has the potential to enable architects to incorporate them as practical artistic components that can be seamlessly integrated into building facades, glazing,

¹School of Microelectronics, Shanghai University, Shanghai, China. ²Materials Genome Institute, Shanghai University, Shanghai, China. ³Shanghai Academy of Fine Arts, Shanghai University, Shanghai, China. ⁴Université de Lille, CNRS, Centrale Lille, Université Polytechnique Hauts-de-France, Junia-ISEN, UMR 8520 - IEMN, Lille, France. ⁵Department of Physics, Research Centre of Excellence for Organic Electronics and Institute of Advanced Materials, Hong Kong Baptist University, Hong Kong, China. ⁶These authors contributed equally: Baozhong Deng, Yi Li. ✉e-mail: xtld@shu.edu.cn; jhzhang@oa.shu.edu.cn; frzhu@hkbu.edu.hk

shading, and other areas^{32–34}. However, transparency of a ST-OSC increases at the expense of its PCE, calling for the identification of materials and cell structures which improve simultaneously both the power generation and the transmission of light for a wide palette of colors and hues. Hence, achieving high-performance ST-OSCs with different colors requires an optimization of optical and electronic properties of the cells through a combination of theoretical simulation, experimental optimization, and process integration. Realization of high-performance translucent color OSCs over competing indexes of PCE, AVT, and hue remains an open challenge. High-throughput optical screening approach is adopted to address the challenge, which allows us to improve understanding of the performance–color relationship and predicting optimal combinations of material choice, device architecture and vibrant hue for producing high-performance translucent color OSCs.

This work reports the effort to develop high-performance translucent color OSCs with a PCE of >15% and a maximum transmittance (T_{\max}) of >20% for three primary colors of red, green and blue. The translucent color OSCs comprise a front transparent indium tin oxide (ITO) electrode, a bulk heterojunction (BHJ) and a rear Ag/dielectric/Ag-based Fabry–Pérot microcavity optical coupling layer. The performance–color relationship of the translucent color OSCs was analyzed using a combination of high-throughput optical simulation to determine the refractive index, thickness of the dielectric layer and hue, allowing light with desired colors to pass through, and yet absorbing the rest of light to generate electricity. By applying this method to high-performance translucent OSCs with a wide palette of colors and hues, the esthetic appeal of their fitting is demonstrated by replicating the vibrant artistic work of Piet Mondrian's "Composition C (1920)". Apart from the power generating functionality, the translucent color OSCs demonstrated in this work are also capable of exhibiting accurate hues and visual attractiveness, providing exciting opportunity and design freedom for applications in BIPV from scientific and artistic perspectives.

Results

High-throughput Optical Screening

The translucent color OSCs comprises a layer configuration of ITO/poly(3,4-ethylenedioxythiophene):poly(styrenesulfonate)(PEDOT:PSS)/BHJ/poly[[2,7-bis(2-ethylhexyl)-1,2,3,6,7,8-hexahydro-1,3,6,8-tetraoxobenz[Imn][3,8]phenanthroline-4,9-diyl]-2,5-thiophenediyl[9,9-bis[3'((N,N-dimethyl)-N-ethylamino)propyl]-9H-fluorene-2,7-diyl]-2,5-thiophenediyl] (PDNIT-F3N)/microcavity optical coupling layer, as shown in Fig. 1a. The BHJ active layer consists of a binary blend film of a polymer donor poly[(2,6-(4,8-bis(5-(2-ethylhexyl-3-fluoro)thiophen-2-yl)-benzo[1,2-b:4,5-b']dithiophene))-alt-(5,5-(1',3'-di-2-thienyl-5',7'-bis(2-ethylhexyl)benzo[1,2-c:4',5'-c'] dithiophene-4,8-dione)] (PM6) and an NFA 2,2'-(2Z,2'Z)-((12,13-bis(2-ethylhexyl)-3,9-(2-butyloctyl)-12,13-dihydro-1,2,5]thiadiazolo [3,4-e]thieno[2',3':4',5']thieno[2',3':4',5']pyrrolo[3,2-g]thieno[2',3':4',5']thieno[3,2-b]indole-2,10-diyl) bis(methanylylidene))bis(5,6-difluoro-3-oxo-2,3-dihydro-1H-indene-2,1-diylidene))dimalononitrile (L8-BO). The absorption spectra measured for the thin films of PM6 and L8-BO are shown in Supplementary Fig. 1. A PM6 layer exhibits an absorption ranging from 450 to 700 nm and a L8-BO layer has a complementary absorption in the NIR wavelength range. A 30 nm-thick PEDOT:PSS hole-transporting layer (HTL) and a 10 nm-thick PDNIT-F3N electron-transporting layer (ETL) are used to assist in efficient charge collection in the translucent color OSCs. The opaque control OSC with a 100 nm-thick Ag upper contact, has been optimized to obtain a PCE of 18.03%, the results are shown in Supplementary Fig. 2 and listed in Supplementary Table 1.

The Fabry–Pérot microcavity optical coupling layer, comprising a layer configuration of Ag/dielectric spacer layer/Ag as shown in the enlarged cross-sectional view in Fig. 1a, is used for enhancing the performance of translucent OSCs over the competing indexes of PCE,

AVT and hue. The optical properties of the translucent OSCs are tuned by adjusting the optical resonance of the microcavity and calculated using the following equation:

$$\sum_i n_i d_i + \frac{\lambda_0(\varphi_1 + \varphi_2)}{4\pi} = m \frac{\lambda_0}{2}, \quad m = 1, 2, 3 \dots \quad (1)$$

where n_i and d_i are the refractive index and the thickness of the i th layer in a multilayer thin film system. λ_0 is the microcavity resonant wavelength. φ_1 and φ_2 are the shift in phase due to the reflection of the faces on the two sides of the dielectric spacer, in this case relating to the thickness of two semitransparent Ag mirrors^{32,33}. The resonance mode of the microcavity optical coupling layer is primarily dependent on the refractive index of the functional layers in the dielectric stack, including ITO, HTL, BHJ, and ETL, and the thicknesses of the semitransparent Ag mirrors. To achieve simultaneously high efficiency and high transparency for the translucent OSCs with different colors, a delicate material selection and thickness optimization of the microcavity optical coupling layer is required. An optical model developed in our previous work^{24,26}, is used to simulate the PCE and the optical transmission of the device. Based on the measured wavelength-dependent refractive indices and extinction coefficients of the functional layers used in the device, as shown in Supplementary Fig. 3, high-throughput optical screening was performed to predict the optimal configuration of the translucent color OSCs over the competing indexes of PCE, visible transparency at the desired wavelengths from the grid that we calculated. The refractive index of dielectric materials varied from 1.0 to 3.0, while the thicknesses of the dielectric layer changed from 0 to 200 nm, and that of the bottom and top Ag mirrors varied from 0 to 100 nm, respectively. The color gamut defined by the dashed locus in the CIE chromaticity diagram in Fig. 1b includes the chromaticity coordinates of 4,632,264 possible cell configurations screened in the calculation. The choices of chromaticity coordinates for red, green, and blue translucent color OSCs are highlighted in the CIE chromaticity diagram as well. The PCE– T_{\max} contour plots obtained for translucent blue, green, and red OSCs are shown in Fig. 1c–e, respectively. The results of high-throughput optical screening reveal that translucent color OSCs with a PCE of >15% and a T_{\max} of >20% can be achieved simultaneously through an appropriate choice of the dielectric indices and thicknesses, e.g., by employing a microcavity structure of Ag (35 nm)/ZnS ($n = 2.3$, 35 nm)/Ag (20 nm) for blue device (blue star symbol), Ag (35 nm)/LaF₃ ($n = 1.6$, 120 nm)/Ag (30 nm) for green device (green star symbol), and Ag (35 nm)/MoO₃ ($n = 2.0$, 108 nm)/Ag (35 nm) for red device (red star symbol).

Performance of Translucent Color OSCs

Guided by the simulated predictions, microcavity optical coupling layers for translucent blue, green, and red OSCs were fabricated. PCE of 16.19%, 15.81%, and 15.67%, along with T_{\max} of 24.07% (at 435 nm), 21.68% (at 549 nm), and 20.11% (at 647 nm), were obtained for translucent blue, green, and red OSCs. The $J-V$ characteristics, external quantum efficiency (EQE), and transmission spectra of the translucent color OSCs are shown in Figs. 1f and 1g, while a comprehensive summary of the photovoltaic parameters is listed in Table 1 and Supplementary Table 2. The surface morphology of a 100 nm thick Ag layer and the microcavities used in the translucent color OSCs are analyzed using scanning electron microscopy (SEM), as shown in Supplementary Fig. 4. The SEM images reveal that the surface of the microcavities used for the translucent blue, green, and red OSCs exhibits similar continuous morphology as compared to that measured for a 100 nm thick Ag layer, ensuring a good conductivity for charge collection in the OSCs. The calculated chromaticity coordinates agree well with the ones measured for the translucent blue, green and red OSCs, as shown in Supplementary Fig. 5. The color appearance of the front and rear sides of the translucent color OSCs are measured. It shows that all

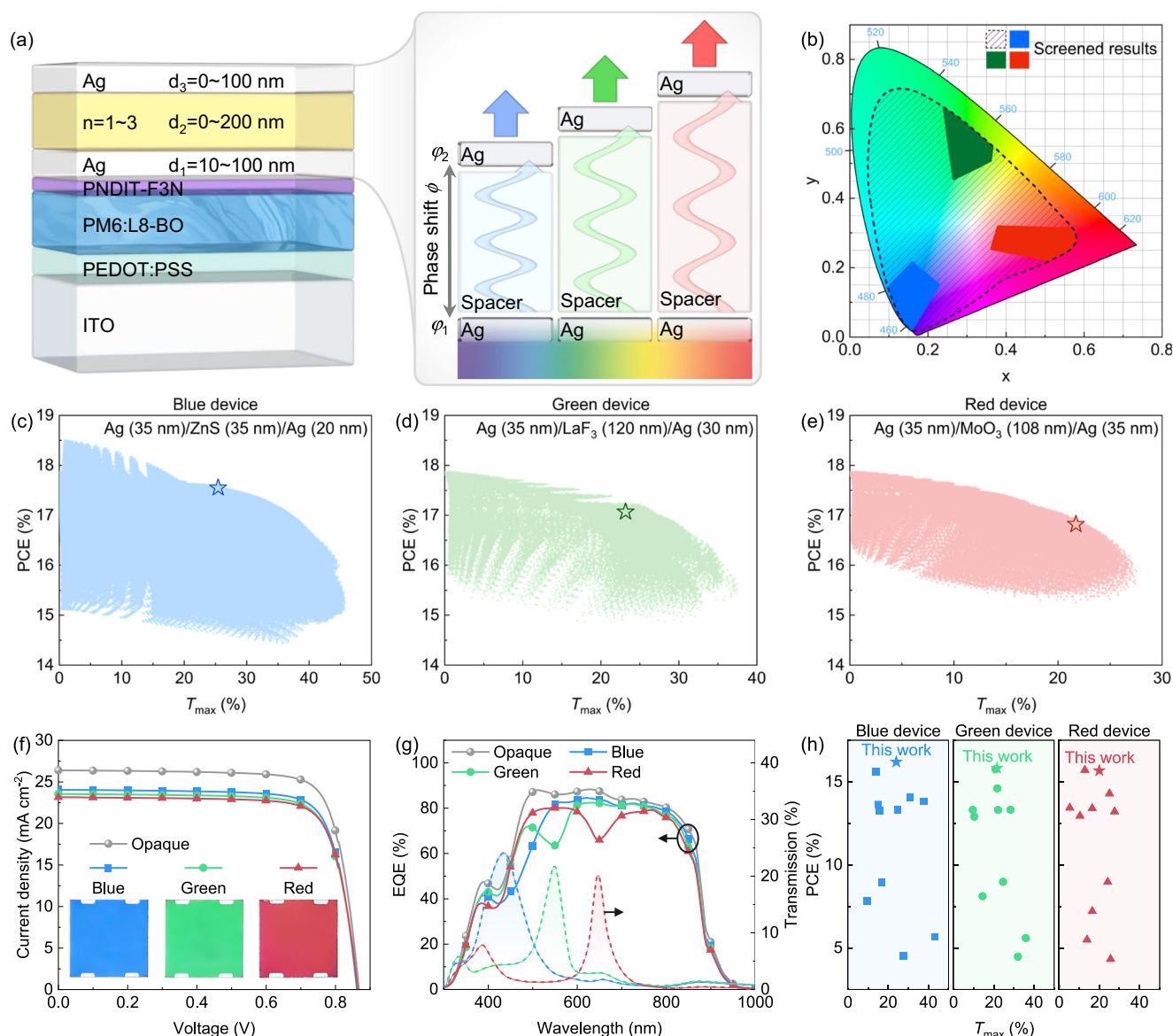


Fig. 1 | High-throughput optical screening. **a** Cross-sectional view of the translucent color OSCs (left) and microcavity optical coupling layer (right). **b** Chromaticity coordinates obtained from high-throughput optical screening (enclosed by dashed line) and the selected results for translucent blue, green, and red OSCs (highlighted in their respective colors). **c–e** Simulated PCE- T_{\max} contour plots obtained for translucent blue, green, and red OSCs, as a function of the refractive index of the dielectric layer and layer thickness of the microcavity optical coupling layers. The star symbols represent the simulated results obtained for the

microcavity optical coupling layers with different configurations of Ag (35 nm)/ZnS (35 nm)/Ag (20 nm) for blue, Ag (35 nm)/LaF₃ (120 nm)/Ag (30 nm) for green and Ag (35 nm)/MoO₃ (108 nm)/Ag (35 nm) for red ST-OSCs. **f** $J-V$ characteristics and **(g)** EQE and transmission spectra measured for the 4.14 mm^2 -sized translucent blue, green, and red OSCs and a control opaque OSC. Inset in **(f)**: photo pictures taken for the corresponding translucent color OSCs. **h** Comparison of PCE and T_{\max} obtained for the translucent blue, green, and red OSCs, juxtaposed with those reported in recent literature listed in Supplementary Table 7.

devices produce a bluish color seen from the back side, as shown in Supplementary Fig. 6. The reflection spectra measured from the front side of the translucent color OSCs were used to calculate the quantum utilization efficiency (QUE), defined as the sum of EQE and transmittance, together with the EQE + T + R spectra, as shown in Supplementary Fig. 7. QUE of the translucent color OSCs is below the transmittance of ITO/glass and the EQE + T + R values remain under 100%, thereby confirming the reliability of our results^{35,36}. The adaptability of the high-throughput optical screening was also used to predict the enhanced performance of the translucent color OSCs, using different polymer:non-fullerene acceptor systems, e.g., PM6:BTP-eC9, over the competing index of PCE, visible transparency and hue. The performance-color relationships obtained for the PM6:BTP-eC9-based translucent red, green, and blue OSCs are shown in Supplementary

Fig. 8. A summary of the results obtained for the PM6:BTP-eC9-based translucent color OSCs is listed in Supplementary Table 3. Comparison of PCE and T_{\max} obtained for the translucent blue, green, and red OSCs reported recently by different groups is shown in Fig. 1h, revealing the enhanced performance of the translucent color OSCs developed in this work.

Translucent blue, green, and red OSCs and control opaque OSCs with different active areas of 4.14 mm^2 and 1.0 cm^2 were fabricated. The 1.0 cm^2 -sized OSCs also possess a PCE of 13–15%, demonstrating the device configuration and design that are capable for the different sizes of translucent color OSCs. $J-V$ characteristics and EQE spectra measured for the 1.0 cm^2 -sized translucent color OSCs and the control opaque OSC are shown in Supplementary Fig. 9 and listed in Supplementary Table 4. Aging tests show that the translucent color OSCs

Table 1 | A summary of the performance of the PM6:L8-BO-based opaque OSCs, and a translucent blue OSC with an upper microcavity optical coupling layer of Ag (35 nm)/ZnS (35 nm)/Ag (20 nm), a translucent green ST-OSC with an upper microcavity optical coupling layer of Ag (35 nm)/LaF₃ (120 nm)/Ag (30 nm), and a translucent red OSC with an upper microcavity optical coupling layer Ag (35 nm)/MoO₃ (108 nm)/Ag (35 nm)

	V_{OC} (V)	J_{SC} (mA cm ⁻²)	J_{cal}^a (mA cm ⁻²)	FF (%)	PCE (%)	T_{max} (%)	Peak (nm)	Color coordinates
Opaque	0.87 ± 0.01	26.39 ± 0.24	25.80	78.95 ± 0.56	18.03 ± 0.19	–	–	–
Blue	0.86 ± 0.01	24.05 ± 0.23	23.65	78.34 ± 0.50	16.19 ± 0.22	24.07	435	(0.1750, 0.1274)
Green	0.86 ± 0.01	23.54 ± 0.12	23.32	77.91 ± 0.57	15.81 ± 0.15	21.68	549	(0.2811, 0.4895)
Red	0.86 ± 0.01	23.14 ± 0.16	22.94	78.67 ± 0.71	15.67 ± 0.23	20.11	647	(0.4547, 0.2841)

The results are averaged from the measurements of 15 OSCs, with an active area of 4.14 mm².

^a J_{cal} calculated using EQE spectra measured for different OSCs.

retained 92% of the initial PCE after stored in a N₂-purged glove box for >800 h, which is more stable as compared to that of the opaque device (86%), as shown in Supplementary Fig. 10a. It reveals that use of an upper microcavity is also favorable for stable operation of the translucent color OSCs. This is because the upper microcavity, comprising a stack of Ag mirror/dielectric spacer/Ag mirror, which acts as a built-in barrier layer to prevent the permeation of moisture and oxygen into the BHJ active layer. The effect of the microcavity on device stability is clearly seen in the accelerated aging test carried out for the translucent color OSCs and the control opaque OSCs in air. The results of light soaking tests, measured for different OSCs under illumination of white LED light source (100 mW/cm²), are shown in Supplementary Fig. 10c.

The performance–color relationship of the translucent color OSCs was analyzed using a combination of theoretical simulation and experimental optimization. The calculated transmission spectra agree well with the ones measured for microcavities used in different translucent color OSCs, as shown in Fig. 2a. Those measured and calculated transmission spectra obtained for the PM6:L8-BO layer and the stack of the glass/HTL/PM6:L8-BO/ETL are shown in Supplementary Fig. 11. The prominent resonance peak locations in different microcavities observed by the measurements agree well with the theoretical simulation. The distribution of the electric field $|E|/|E_0|^2$ in the translucent color OSCs was also calculated, the results are shown in Fig. 2b. An enhanced intensity of the electric field within the microcavity is observed, resulting from optical interference. There is an obvious decrease in field intensity at resonance wavelength, due to the high transmittance. The exciton generation rate in the translucent blue, green, and red OSCs and the control opaque OSC was also examined. The results are shown in Supplementary Fig. 12. The difference in exciton generation rate in these OSCs is shown in Fig. 2c, which remains approximately zero except for negative values at the respective resonance wavelength. By optimizing the microcavity configuration, the exciton generation rate in the translucent color OSCs can be optimized for achieving high efficiency.

The fusion of art and power in OSCs

The esthetic appeal of the translucent color OSCs is explored and demonstrated by replicating an artwork which functions simultaneously as a photovoltaic element and an architectural embellishment. A photo picture taken for an iconic masterpiece “Composition C” (Fig. 3a) of Piet Mondrian, who is well-known in the development of modern abstract art. In his quintessential abstract creations, especially those from the 1920s, Piet Mondrian distilled his forms to lines and rectangles and, more importantly, his color scheme to basic elements, forging a universal visual language^{37,38}. Using high-throughput optical screening, a range of translucent color OSCs was selected to match the hues of the original artwork, including navy, sky blue, azure, yellow, vermilion, and brown colors, as shown in Fig. 3b. The corresponding configurations of the microcavity optical coupling layers are listed in Supplementary Table 5. The transmission spectra measured for the translucent navy, sky-blue, azure, yellow, vermilion, and brown OSCs are shown in Fig. 3c, revealing artistic features of the translucent OSCs.

The corresponding J – V characteristics and EQE spectra measured for the 1.0 cm²-sized translucent color OSCs with a PCE over the range from 10 to 15%, are shown in Supplementary Fig. 13. A summary of PCE, T_{max} , and chromaticity coordinates obtained for the translucent navy, sky-blue, azure, yellow, vermilion, and brown OSCs is listed in Supplementary Table 6. The reflection spectra, QUE and EQE + T + R obtained for these translucent color OSCs are shown in Supplementary Fig. 14 and Supplementary Fig. 15. The 10 × 10 cm²-sized translucent color OSC modules were prepared using the slot-die coating, overlaid microcavity optical coupling layers for different colors using multi-step evaporation process, as illustrated schematically in Fig. 3d. A photo picture taken for a 10 × 10 cm²-sized translucent color OSC module comprising sub-cells having different shapes and colors is shown in Supplementary Fig. 16, revealing a wide palette of colors and well replicating Piet Mondrian’s artwork “Composition C (1920)”. The schematic flow of the device fabrication processes including slot-die coating and multi-step evaporation process for sub-microcavities having different shapes and colors are illustrated in Supplementary Fig. 17 and Supplementary Fig. 18. The thickness, uniformity and homogeneity of the functional layers of the PEDOT:PSS HTL and PM6:L8-BO blend layer used in the 10 × 10 cm²-sized translucent OSC module was optimized by controlling the injection rate in the slot-die coating process, as shown Supplementary Fig. 19. A movie recorded for a 10 × 10 cm²-sized translucent color OSC module, replicating the patterns of Piet Mondrian’s artwork “Composition C (1920)” and generating electricity to power a digital clock under daylight, is shown in Supplementary Movie 1. The device architecture and design approach demonstrated in this work are very encouraging, demonstrating the art and science of translucent color OSCs for various applications in power-generating windows, mobile electronics, smart sensors, automotive, and green-houses. An envision of potential BIPV installations utilizing translucent color OSCs is shown in Supplementary Fig. 20.

In summary, the artistic and scientific perspectives of the translucent color OSCs are explored over the competing indexes of efficiency, transparency and vibrant hue using a combination of high-throughput optical screening and experimental optimization. The approach offers significant creative freedom in the design of OSCs. The successful replication of Piet Mondrian’s “Composition C (1920)” using a 10 × 10 cm²-sized translucent color OSC module with competitive efficiency, average visible transmittance, and hue, bridges art and technology in OSCs for a plethora of applications in BIPV that harmonizes power generating windowpanes and building facades with a very high degree of esthetic appeals and versatility.

Methods

Materials

PM6, L8-BO, and PNDIT-F3N were purchased from Organtec Ltd. PEDOT:PSS, the Clivious P VP Al 4083, was purchased from Xi’an Yuri Solar Co., Ltd. DIO was purchased from Sigma–Aldrich. ZnS and LaF₃ were purchased from Adamas. MoO₃ was purchased from Fuzhou Innovation Photoelectric Technology Co., Ltd. The chemicals and reagents were used as received.

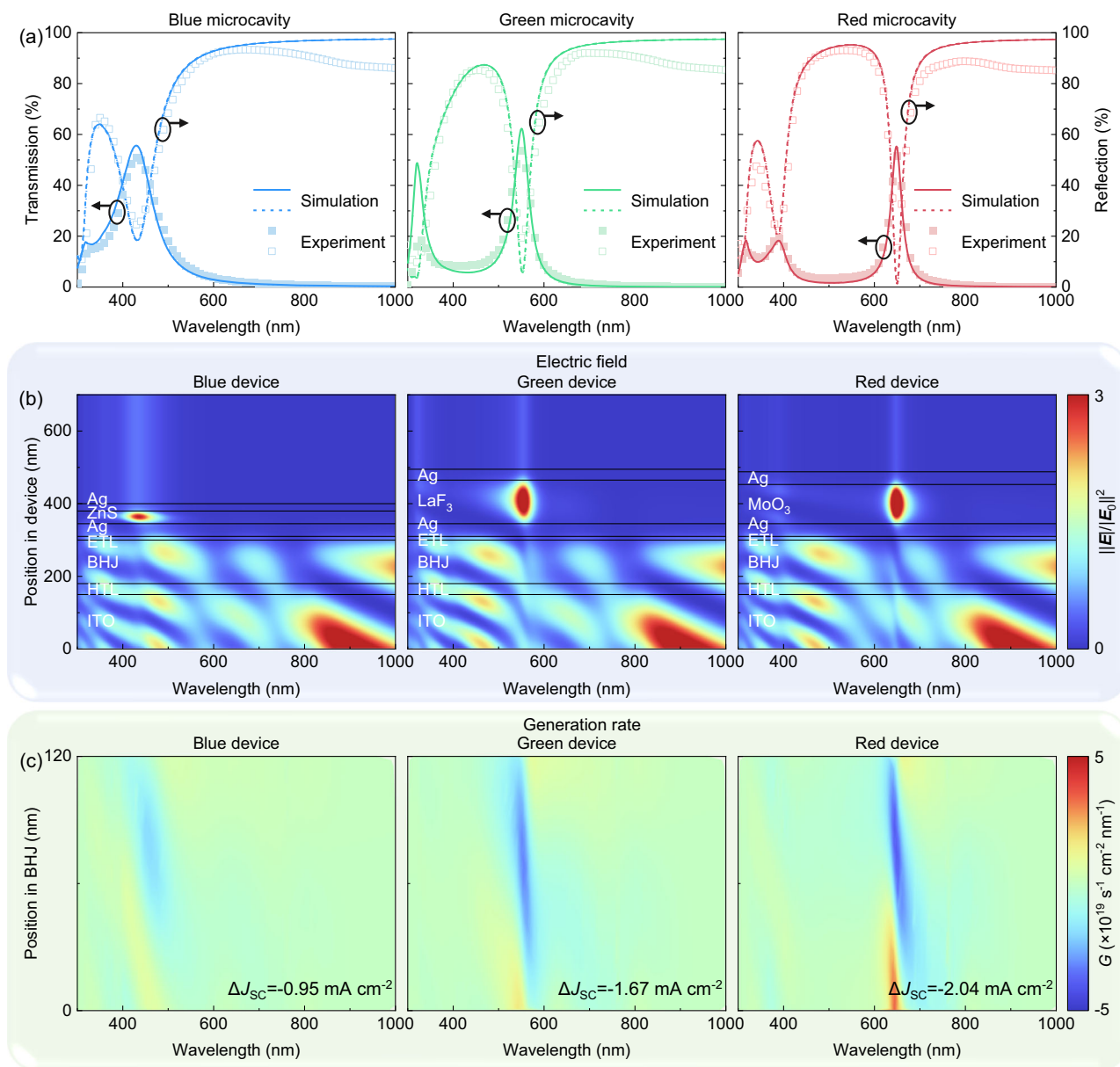


Fig. 2 | Optical profile of the translucent color OSCs. a The calculated and measured transmission and reflection spectra of the microcavity optical coupling layers used in translucent blue, green and red OSCs. **b** The calculated electric field

distribution profiles in the translucent blue, green, and red OSCs. **c** Comparison of the exciton generation rate (G) in an opaque OSC and in the translucent blue, green, and red OSCs.

Device Fabrication

The ITO/glass substrates, with a sheet resistance of $15 \Omega/\text{sq}$, were subjected to a series of ultrasonic cleaning steps. Each step involved utilizing detergent, deionized water, acetone, and isopropyl alcohol, with each step lasting 30 min. Following the wet cleaning process, the wet-cleaned ITO/glass substrates were treated by oxygen plasma for 6 min prior to the device fabrication. A 30 nm-thick PEDOT:PSS HTL was coated on ITO/glass substrates using spin coating at a rotation speed of 3000 rpm for 30 s. Subsequently, the PEDOT:PSS/ITO/glass substrates were annealed at 130°C for 10 min in air. The PM6:L8-BO solution was formulated by dissolving PM6 and L8-BO in chloroform (1:1.2 w/w, 16 mg ml^{-1}) with a 0.5 v/v of DIO at 40°C for 2 h. The PM6:L8-BO BHJ was deposited on the PEDOT:PSS HTL using spin-coating, using an optimal rotation speed of 3500 rpm for 30 s. This was followed by an annealing process at 110°C for 10 min in a glove box, with oxygen and moisture levels below 0.01 ppm. Following that, a 10 nm thick PNDIT-F3N ETL, 0.95 mg ml^{-1} in methanol with a 5 v/v acetic acid

cosolvent, was applied onto the BHJ active layer using spin-coating at a rotational speed of 3000 rpm for 30 s. The microcavity optical coupling layer was formed using thermal evaporation in a vacuum system, with a base pressure of $<5 \times 10^{-4} \text{ Pa}$. The evaporation rate for Ag was 2.0 \AA s^{-1} , and that for dielectric layers was 3.0 \AA s^{-1} . The translucent color OSCs with two different effective areas of 4.14 mm^2 and 1.0 cm^2 , defined by the overlap area between the front ITO contact and the rear metal electrode, were made. The 1.0 cm^2 -sized OSCs were fabricated using dynamic spin-coating method. In the dynamic spin coating process, the rotation acceleration time was 3 s, and the solution was dispensed at the 1 s mark during the acceleration phase. The dispensing of the solution is completed within 0.5 to 1 s.

The largest-area ST-OSC module was fabricated on a $10 \times 10 \text{ cm}^2$ -sized glass substrate using a slot-die coater (RD coater-H200, Hunan NanoUp Electronics Technology Co., Ltd). For slot-die coated devices, the concentration of the PM6:L8-BO solution was adjusted to 10 mg mL^{-1} (1:1.2 w/w), to ensure good fluidity and prevent clogging by

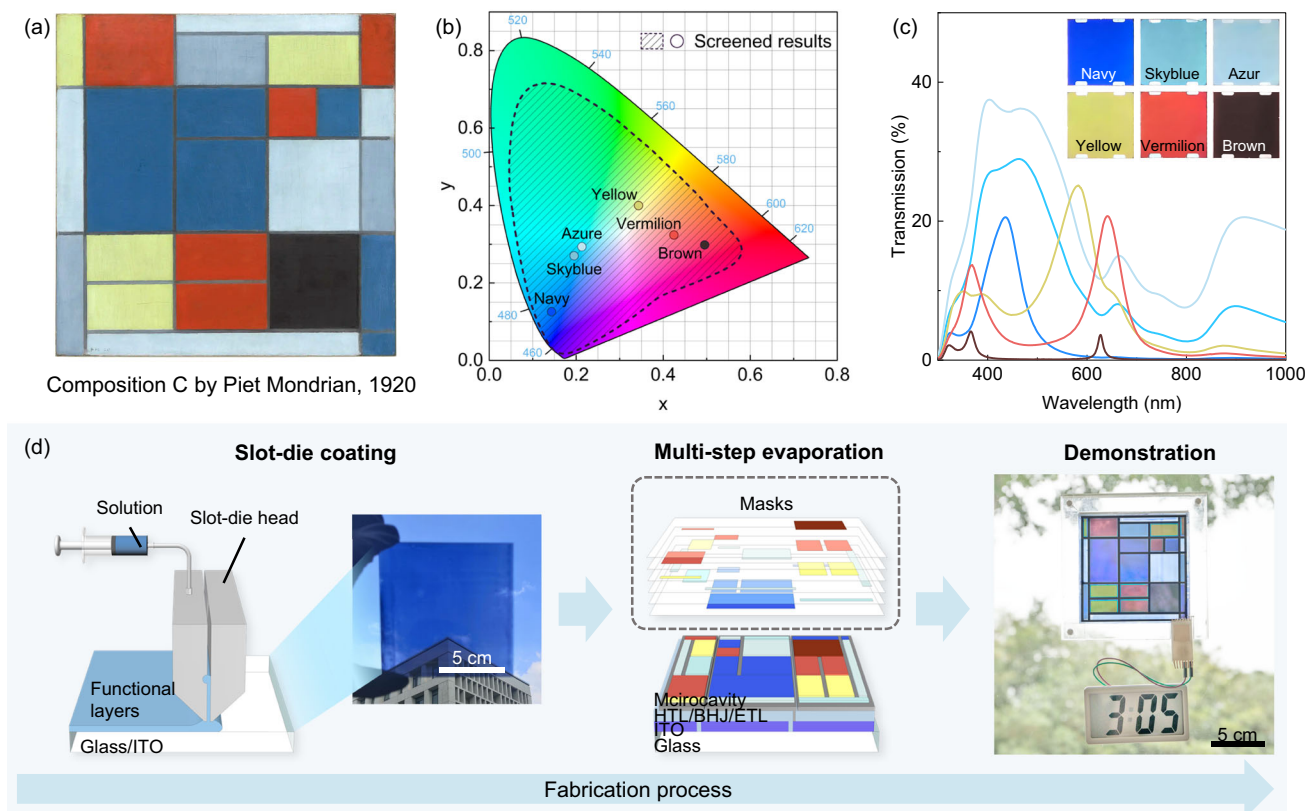


Fig. 3 | The art of translucent color OSCs. **a** A photo picture taken for Piet Mondrian's artwork "Composition C (1920)". **b** The chromaticity coordinates and **(c)** the transmission spectra of the translucent navy, sky-blue, azure, yellow, vermilion, and brown OSCs, inset: photo pictures taken for different translucent OSCs. **d** Schematic diagram illustrating the fabrication process of the translucent color

OSC module. Insets: a photo picture taken for a slot-die coated film (left), and a photo picture taken for a translucent OSC module (right) revealing a wide palette of colors and hues, well replicating Piet Mondrian's artwork "Composition C (1920)", and powering a digital clock.

precipitated particles. The width (d) of the film is determined by the following equation:

$$d = \frac{Q}{W \times U \rho} \quad (2)$$

where Q is the injection rate, W is the width of coating (10 cm), U is the coating speed, c is the solution concentration and ρ is volumetric density of the coated material in the form. The detailed slot-die coating process is illustrated in Supplementary Fig. 17. The shim width of slot-die coating was 0.7 mm. The gap between the slot-die head and the substrate was 0.15 mm for HTL and ETL, and that for the active layer was 0.4 mm. The solution injection speed was 2 mL min⁻¹ for HTL and ETL, and 8 mL min⁻¹ for the active layer. The coating speed was 15 mm s⁻¹ for all functional layers. In the slot-die coating process, the substrate length was 10 cm. The injection was stopped at the 8.0 cm mark, using the remaining ink to complete the rest 2.0 cm-long film. This approach helps prevent liquid accumulation for undesired increase in film thickness or overflowing near the margin of the substrate. All parameters were delicately optimized to prevent the formation of the holes and cracks, leading to the uniform and homogeneous films. The functional layers were divided manually to ensure the connection of adjacent sub-cells.

To ensure uniform evaporation across the large-area substrate, the mask (containing the substrate) was placed directly above the heated crucible (containing Ag or dielectric materials). During the evaporation process, the mask was kept in constant rotation. A 6 MHz gold-coated quartz crystal was positioned near the mask to monitor the film thickness. The patterned microcavity optical coupling layers were fabricated using a total of 6 masks, each corresponding to a different color, as

shown in Supplementary Fig. 18. Initially, a layer of Ag covering the full electrode area was deposited. For each color, the process involved three sequential evaporation steps: Ag/dielectric/Ag. In total, this multi-step selective-area evaporation required 19 evaporation cycles.

Characterization

The transmission and absorption spectra of the samples were measured using a UV-vis spectrophotometer (MAPADA UV-1800PC). The CIE 1931 chromaticity coordinates of the translucent color OSCs were measured using a PR-655 spectroradiometer (Photo Research). The $J-V$ characteristics of the OSCs were measured in a N₂-purged glove box at 25 °C. The EQE spectra of the OSCs were measured at 25 °C and 40% relative humidity. The $J-V$ characteristics of the translucent color OSCs were measured under illumination of an AM1.5 G solar simulator (Newport Oriel Sol3A), calibrated with a power density of 100 mW cm⁻², from ITO side of the OSCs using a source meter (Keithley 2420). A metal aperture mask with an active area of 4.14 mm² or 1.0 cm² was used in the measurement of the OSCs. EQE and reflection spectra of the OSCs were measured using a 7-SCSpec solar cell measurement system (Beijing Saifan Optoelectronic Instrument Co., Ltd). The beam employed was a 210-Hz chopped, monochromate, and focused beam from a Xe lamp. The beam is concentrated to underfill the area of the device. The surface morphology of the functional layers was analyzed using a ZEISS GeminiSEM 300 high-resolution field emission scanning electron microscope (SEM).

Theoretical Simulation

Optical constants for functional layers were measured using a spectroscopic ellipsometer (J.A. Woollam RC2-XI). Wavelength-dependent

transmission, $T(\lambda)$, absorption, $A(\lambda)$, and profile of the electric field, $E(x, \lambda)$, in the translucent color OSCs were simulated using the transfer matrix method over the wavelength range from 300 to 1000 nm.

In the simulation, considering an incoming light from the glass side and normal to the cell, the functional layers are considered as a homogeneous media with wavelength-dependent optical constants. The calculation is based on transfer matrix method:

$$\mathbf{M} = \begin{pmatrix} \cos\left(\frac{2\pi}{\lambda}\tilde{N}d\right) & \frac{i}{N}\sin\left(\frac{2\pi}{\lambda}\tilde{N}d\right) \\ i\tilde{N}\sin\left(\frac{2\pi}{\lambda}\tilde{N}d\right) & \cos\left(\frac{2\pi}{\lambda}\tilde{N}d\right) \end{pmatrix} \quad (3)$$

where $\tilde{N} = n - ik$ is the complex refractive index of a functional layer, comprising a real part n (refractive index) and an imaginary part k (extinction coefficient), d is the thickness of a functional material. \mathbf{M} is the transfer matrix of a functional in a multi-layered system. The total transfer matrix of the system is obtained by multiplying the transfer matrix of each layer:

$$\mathbf{M}_{\text{total}} = \mathbf{M}_1 \mathbf{M}_2 \mathbf{M}_3 \cdots \quad (4)$$

The absorption of the active layer, $A(\lambda)$, is calculated considering the forward and backward propagating electromagnetic waves, and the interference between the forward and backward propagating electromagnetic waves in the layer:

$$A(\lambda) = \frac{2\pi}{\lambda n_{\text{in}}} \text{Im}(\tilde{N}) \left[|E_+|^2 f_+ + |E_-|^2 f_- + \frac{|E_+||E_-|}{k_z} (\sin(2k'_z b + \phi) - \sin(2k'_z a + \phi)) \right] \quad (5)$$

where n_{in} is the refractive index of the incident medium. E_+ and E_- are the forward and backward propagating electric field components in the layer. f_+ and f_- are functions related to the imaginary part of the wavevector k'_z :

$$\begin{cases} k'_z \neq 0 : f_+ = \frac{e^{-2k'_z a} - e^{-2k'_z b}}{2k'_z}, f_- = \frac{e^{2k'_z b} - e^{2k'_z a}}{2k'_z} \\ k'_z = 0 : f_+ = f_- = b - a \end{cases} \quad (6)$$

k'_z is the real part of the wavevector, which describes the propagation constant in the layer. a and b are the start and end boundaries of the layer. ϕ is the phase difference between the forward and backward electric fields, given by:

$$\phi = \arg(E_+ E_-^*) \quad (7)$$

The transmission, $T(\lambda)$ is calculated considering the electric field strength of the transmitted wave:

$$T(\lambda) = |E_{\text{trans}}|^2 \frac{\text{Re}(k_{z,\text{out}})}{\text{Re}(k_{z,0})} \quad (8)$$

where E_{trans} is the transmitted wave component in the last medium. $k_{z,0}$ and $k_{z,\text{out}}$ is the wavevector component in the incident medium and the output medium, respectively. $A(\lambda)$ and $T(\lambda)$ are then used for calculating PCE, T_{max} , and chromaticity coordinates of the translucent color OSCs.

Assuming an internal quantum efficiency of 100%, the simulated short current density J_{cal} is derived from the $A(\lambda)$ spectra. Additionally, the simulated PCE is computed using the formula $\text{PCE} = J_{\text{cal}} \times V_{\text{OC}} \times \text{FF}$, where the V_{OC} and FF are considered constant at $V_{\text{OC}} = 0.86$ V and $\text{FF} = 0.79$, respectively.

The simulated chromaticity coordinates were calculated using the following equations:

$$\begin{cases} x = \frac{X}{X+Y+Z} \\ y = \frac{Y}{X+Y+Z} \end{cases} \quad (9)$$

where X , Y , and Z are the tristimulus values, calculated using the following equations:

$$\begin{cases} X = \int_{380}^{780} F(\lambda) T(\lambda) \bar{x}(\lambda) d\lambda \\ Y = \int_{380}^{780} F(\lambda) T(\lambda) \bar{y}(\lambda) d\lambda \\ Z = \int_{380}^{780} F(\lambda) T(\lambda) \bar{z}(\lambda) d\lambda \end{cases} \quad (10)$$

where $F(\lambda)$ is the AM1.5 G irradiation, $\bar{x}(\lambda)$, $\bar{y}(\lambda)$ and $\bar{z}(\lambda)$ are the color matching functions specified by the International Commission on Illumination.

In the high throughput computing for device structure: ITO (150 nm)/HTL (30 nm)/BHJ (120 nm)/ETL (10 nm)/Ag_{bottom}/dielectric layer/Ag_{top}. The calculations were performed using the algorithm written in Python code. NumPy library was imported for its powerful vectorization and broadcasting ability, ensuring highly efficient computation. For the high-throughput computing, the layer thicknesses and refractive index (noted as d_1 , d_2 , d_3 , n) are defined as variables and varied in a grid using `numpy.arange` function. The total combinations are generated using `numpy.meshgrid` function, eliminating the need for expliciting loops and significantly enhancing computation speed. The dielectric materials are selected from the ones with desired refractive index and layer thickness that can be easily processed, e.g., using thermal evaporation, for achieving enhanced performance of translucent color OSCs over the competing indexes of PCE, visible transparency, and chromaticity coordinates for replicating the color fidelity and patterns of Piet Mondrian's artwork "Composition C (1920)". The refractive index of dielectric materials was constant across different wavelengths, ranging from 1.0 to 3.0, with a precision of 0.1. The thickness of the dielectric layer stack varied from 0 to 200 nm, with a 2.0 nm interval. The thickness of the bottom Ag mirror, also acting as the electrode, varied over the thickness range from 10 to 95 nm, whereas the thickness of the top Ag mirror varied over the thickness range from 0 to 95 nm. An increment interval of 1.0 nm was used when the thickness of the Ag mirror is <40 nm, an increment of 5 nm was used when while its thickness is >40 nm. A comprehensive analysis was conducted for 4,632,264 possible translucent color OSCs over the competing indexes of PCE, T_{max} and chromaticity coordinates. The data was processed using Matplotlib library. The schematic flow of the high-throughput optical screening computing process is illustrated in Supplementary Fig. 21. Translucent color OSCs and their chromaticity coordinates in the CIE chromaticity diagram, predicated by the high-throughput optical screening for the desired colors, are shown in Supplementary Fig. 22.

Reporting Summary

Further information on research design is available in the Nature Research Reporting Summary linked to this article.

Data availability

The data that support the findings of this study are presented in the main text and Supplementary Information file. All the data are available from the corresponding authors on request.

References

- Ritzer, D. B. et al. Translucent perovskite photovoltaics for building integration. *Energy Environ. Sci.* **16**, 2212–2225 (2023).
- Gauch, H. L., Dunant, C. F., Hawkins, W. & Cabrera Serrenho, A. What really matters in multi-storey building design? A simultaneous

- sensitivity study of embodied carbon, construction cost, and operational energy. *Appl. Energy* **333**, 120585 (2023).
3. Kuhn, T. E. et al. Review of technological design options for building integrated photovoltaics (BIPV). *Energy Build.* **231**, 110381 (2021).
 4. Traverse, C. J., Pandey, R., Barr, M. C. & Lunt, R. R. Emergence of highly transparent photovoltaics for distributed applications. *Nat. Energy* **2**, 849–860 (2017).
 5. Kannan, N. & Vakeesan, D. Solar energy for future world:—a review. *Renew. Sust. Energy Rev.* **62**, 1092–1105 (2016).
 6. Ballif, C., Perret-Aebi, L.-E., Lufkin, S. & Rey, E. Integrated thinking for photovoltaics in buildings. *Nat. Energy* **3**, 438–442 (2018).
 7. Wang, D. et al. High-performance see-through power windows. *Energy Environ. Sci.* **15**, 2629–2637 (2022).
 8. Xu, X. et al. Efficient semitransparent organic solar cells with CRI over 90% enabled by an ultralow-bandgap A-DA'D-A small molecule acceptor. *Adv. Funct. Mater.* **34**, 2305017 (2024).
 9. Yuan, X. et al. Simultaneous enhanced device efficiency and color neutrality in semitransparent organic photovoltaics employing a synergy of ternary strategy and optical engineering. *Adv. Funct. Mater.* **32**, 2200107 (2022).
 10. Li, Y., Huang, X., Sheriff, H. K. M. & Forrest, S. R. Semitransparent organic photovoltaics for building-integrated photovoltaic applications. *Nat. Rev. Mater.* **8**, 186–201 (2022).
 11. Cheng, H., Zhao, Y. & Yang, Y. Toward high-performance semitransparent organic photovoltaics with narrow-bandgap donors and non-fullerene acceptors. *Adv. Energy Mater.* **12**, 2102908 (2022).
 12. Wang, D. et al. High-performance semitransparent organic solar cells with excellent infrared reflection and see-through functions. *Adv. Mater.* **32**, 2001621 (2020).
 13. Fu, J. et al. Rational molecular and device design enables organic solar cells approaching 20% efficiency. *Nat. Commun.* **15**, 1830 (2024).
 14. He, X. et al. Selenium substitution for dielectric constant improvement and hole-transfer acceleration in non-fullerene organic solar cells. *Nat. Commun.* **15**, 2103 (2024).
 15. Yoon, S. et al. High-performance scalable organic photovoltaics with high thickness tolerance from 1 cm² to above 50 cm². *Joule* **6**, 2406–2422 (2022).
 16. Jiang, K. et al. Suppressed recombination loss in organic photovoltaics adopting a planar-mixed heterojunction architecture. *Nat. Energy* **7**, 1076–1086 (2022).
 17. Deng, B. et al. Niobium-Carbide MXene Modified Hybrid Hole Transport Layer Enabling High-Performance Organic Solar Cells Over 19. *Small* **19**, 2207505 (2023).
 18. Xie, D. et al. A 2.20 eV Bandgap Polymer Donor for Efficient Colorful Semitransparent Organic Solar Cells. *Adv. Funct. Mater.* **33**, 2212601 (2023).
 19. Liu, X., Zhong, Z., Zhu, R., Yu, J. & Li, G. Aperiodic band-pass electrode enables record-performance transparent organic photovoltaics. *Joule* **6**, 1918–1930 (2022).
 20. Guan, S. et al. Balancing the selective absorption and photon-to-electron conversion for semitransparent organic photovoltaics with 5.0% light-utilization efficiency. *Adv. Mater.* **34**, 2205844 (2022).
 21. Huang, X. et al. A molecular weight-regulated sequential deposition strategy enabling semitransparent organic solar cells with the light utilization efficiency of over 5%. *Energy Environ. Sci.* **15**, 4776–4788 (2022).
 22. Xu, T. et al. High-performance semitransparent organic solar cells: from competing indexes of transparency and efficiency perspectives. *Adv. Sci.* **9**, 2202150 (2022).
 23. Deng, B. et al. Multifunctional semitransparent organic photovoltaics with high-throughput screened infrared reflector. *ACS Energy Lett.* **9**, 976–984 (2024).
 24. Xu, T. et al. High-throughput computing guided low/high index optical coupling layer for record-performance semitransparent organic solar cells. *Adv. Energy Mater.* **13**, 2301367 (2023).
 25. Xia, R., Brabec, C. J., Yip, H.-L. & Cao, Y. High-throughput optical screening for efficient semitransparent organic Solar Cells. *Joule* **3**, 2241–2254 (2019).
 26. Ng, G. et al. Optical enhancement in semitransparent polymer photovoltaic cells. *Appl. Phys. Lett.* **90**, 103505 (2007).
 27. Liang, N. et al. Trans-reflective structural color filters assisting multifunctional-integrated semitransparent photovoltaic window. *Adv. Mater.* **35**, 2300360 (2023).
 28. Liu, X. et al. High-performance colorful organic photovoltaics with microcavity resonance color filter. *Adv. Energy Mater.* **13**, 2301361 (2023).
 29. Xu, C. et al. Colorful semitransparent organic photovoltaics with record key parameters by optimizing photon utilization and Fabry-Pérot resonator electrode. *Adv. Opt. Mater.* **12**, 2302285 (2024).
 30. Li, X. et al. Semitransparent organic solar cells with vivid colors. *ACS Energy Lett.* **5**, 3115–3123 (2020).
 31. Chen, Y.-H. et al. Microcavity-embedded, colour-tuneable, transparent organic solar cells. *Adv. Mater.* **26**, 1129–1134 (2014).
 32. Xiao, L. et al. Semitransparent organic solar cells with homogeneous transmission and colorful reflection enabled by an ITO-free microcavity architecture. *Adv. Mater.* **36**, 2303844 (2024).
 33. Bing, J. et al. Perovskite solar cells for building integrated photovoltaics-glazing applications. *Joule* **6**, 1446–1474 (2022).
 34. Chang, S.-Y., Cheng, P., Li, G. & Yang, Y. Transparent polymer photovoltaics for solar energy harvesting and beyond. *Joule* **2**, 1039–1054 (2018).
 35. Zhang, Y. et al. Guided-growth ultrathin metal film enabled efficient semi-transparent organic solar cells. *Adv. Energy Mater.* **13**, 2203266 (2023).
 36. Sun, S. et al. Solution processed semi-transparent organic solar cells over 50% visible transmittance enabled by silver nanowire electrode with sandwich structure. *Adv. Mater.* **35**, 2305092 (2023).
 37. Van Sark, W. et al. The “Electric Mondrian” as a luminescent solar concentrator demonstrator case study. *Sol. RRL* **1**, 1600015 (2017).
 38. Gamwell, L. & deGrasse Tyson, N. *Exploring the Invisible: Art, Science, and the Spiritual*. (Princeton University Press, 2020).

Acknowledgements

B.D. and Y.L. contributed equally to this work. T.X. acknowledges the support from the National Natural Science Foundation of China (12174244). F.Z. acknowledges the support from the Research Grants Council, University Grants Committee, Hong Kong, General Research Fund (12302623, 12304024), NSFC/RGC Joint Research Scheme (N_HKBU201/19), and Hong Kong Innovation and Technology Fund (GHP-121-21GD).

Author contributions

F.Z. supervised the execution of the project. J.Z. and T.X. conceived this project and designed the experiments. B.D., Z.L. and K.Z. fabricated the devices. B.D. and S.W. measured the photovoltaic performances of the devices. Y.L. fabricated the OSC module. X.L. conducted the replication of the artwork. B.D. and B.G. performed theoretical simulations and analyzes. B.D., Y.L., T.X., B.G., and F.Z. drafted and finalized the manuscript. All authors participated in the discussions for manuscript preparation.

Competing interests

The authors declare no competing interests.

Additional information

Supplementary information The online version contains supplementary material available at <https://doi.org/10.1038/s41467-025-55924-9>.

Correspondence and requests for materials should be addressed to Tao Xu, Jianhua Zhang or Furong Zhu.

Peer review information *Nature Communications* thanks Huiqiong Zhou and the other anonymous reviewer(s) for their contribution to the peer review of this work. A peer review file is available.

Reprints and permissions information is available at <http://www.nature.com/reprints>

Publisher's note Springer Nature remains neutral with regard to jurisdictional claims in published maps and institutional affiliations.

Open Access This article is licensed under a Creative Commons Attribution-NonCommercial-NoDerivatives 4.0 International License, which permits any non-commercial use, sharing, distribution and reproduction in any medium or format, as long as you give appropriate credit to the original author(s) and the source, provide a link to the Creative Commons licence, and indicate if you modified the licensed material. You do not have permission under this licence to share adapted material derived from this article or parts of it. The images or other third party material in this article are included in the article's Creative Commons licence, unless indicated otherwise in a credit line to the material. If material is not included in the article's Creative Commons licence and your intended use is not permitted by statutory regulation or exceeds the permitted use, you will need to obtain permission directly from the copyright holder. To view a copy of this licence, visit <http://creativecommons.org/licenses/by-nc-nd/4.0/>.

© The Author(s) 2025